Nano Research

ISSN 1998-0124 CN 11-5974/O4
https://doi.org/10.1007/s12274-018-2194-6

Research Article

Space-confined growth of monolayer $ReSe_2$ under a graphene layer on Au foils

Chunyu Xie[1,2,§], Shaolong Jiang[1,2,§], Xiaolong Zou[3,§], Yuanwei Sun[4,5], Liyun Zhao[1], Min Hong[1,2], Shulin Chen[4,6], Yahuan Huan[1,2], Jianping Shi[1,2], Xiebo Zhou[1,2], Zhepeng Zhang[1,2], Pengfei Yang[1,2], Yuping Shi[1,2], Porun Liu[7], Qing Zhang[1], Peng Gao[4,5,8], and Yanfeng Zhang[1,2] (✉)

[1] *Department of Materials Science and Engineering, College of Engineering, Peking University, Beijing 100871, China*
[2] *Center for Nanochemistry (CNC), Beijing National Laboratory for Molecular Sciences, College of Chemistry and Molecular Engineering, Peking University, Beijing 100871, China*
[3] *Tsinghua-Berkeley Shenzhen Institute (TBSI), Tsinghua University, Shenzhen 518055, China*
[4] *Electron Microscopy Laboratory, School of Physics, Peking University, Beijing 100871, China*
[5] *International Center for Quantum Materials, School of Physics, Peking University, Beijing 100871, China*
[6] *State Key Laboratory of Advanced Welding and Joining, Harbin Institute of Technology, Harbin 150001, China*
[7] *Centre for Clean Environment and Energy, Griffith University, Gold Coast 4222, Australia*
[8] *Collaborative Innovation Center of Quantum Matter, Beijing 100871, China*
[§] *Chunyu Xie, Shaolong Jiang, and Xiaolong Zou contributed equally to this work.*

Received: 28 June 2018 / **Revised:** 9 August 2018 / **Accepted:** 4 September 2018

ABSTRACT

Vertical heterostructures based on two-dimensional (2D) materials have attracted widespread interest for their numerous applications in electronic and optoelectronic devices. Herein, we report the direct construction of an abnormal graphene/$ReSe_2$ stack on Au foils by a two-step chemical vapor deposition (CVD) strategy. During the second growth stage, monolayer $ReSe_2$ is found to preferentially evolve at the interface between the first-grown graphene layer and the Au substrate. The unusual stacking behavior is unraveled by *in-situ* "cutting open" the upper graphene from the defects to expose the lower $ReSe_2$ using scanning tunneling microscopy (STM). From combination of these results with density functional theory calculations, the domain boundaries and edge sites of graphene are proposed to be adsorption sites for Re and Se precursors, further facilitating the growth of $ReSe_2$ at the van der Waals gap of graphene/Au. This work hereby offers an intriguing strategy for obtaining vertical 2D heterostructures featured with an ultra-clean interface and a designed stacking geometry.

KEYWORDS

graphene, rhenium selenide, chemical vapor deposition, scanning tunneling microscopy, two-dimensional (2D) heterostructure

1 Introduction

Vertically stacked van der Waals (vdW) heterostructures based on the stacking of graphene (Gr) and monolayer transition metal dichalcogenides (TMDCs, such as MoS_2 and WSe_2) have attracted extensive scientific interests due to the induced novel physical phenomena, such as the inverse spin galvanic effect, superconductivity, etc. [1, 2]. More intriguingly, various intriguing applications have been developed with such heterostructures, especially in field-effect transistors [3, 4], large-scale electronic systems [5], light-emitting diodes [6], photodetectors [7, 8], phototransistor [9], efficient catalysis [10], etc.

However, the popular layer-by-layer stacking route for heterostructure construction based on the mechanically-exfoliated two-dimensional (2D) thin films usually results in interfacial contamination, uncontrollable domain size, random orientation, along with an unsatisfactory device performance [11–14]. To avoid the transfer process, a direct chemical vapor deposition (CVD) route was developed to synthesize MoS_2/Gr and MoS_2/hexagonal boron nitride (h-BN) heterostructures on Cu [15], Au [16, 17] and sulfide-resistant nickel-based alloys [18] or to introduce TMDCs on a pre-transferred Gr or h-BN layer (derived from CVD or exfoliation) on insulating substrates [19–22]. In these cases, the vertical stacks usually followed the deposition sequence of the composite layers.

It is worthy of reminding that, metal atoms or small molecules can be trapped into the interfaces between 2D materials and their substrates with the subsequent formation of monolayers. For example, Au was intercalated into the interfaces between Gr and a Ni or SiC substrate to obtain the intrinsic electronic structure of Gr [23, 24]. In addition, the intercalations of alkali metals (Li and Cs, etc.) [25, 26] and transition metals (Fe and Mn, etc.) [27–29] were also performed to tune the coupling of Gr to substrates, such as SiC, Ni and Ir. Additionally, small molecules such as H_2 [30], O_2 [31, 32], H_2O [33] and CO [34, 35] were also observed to be able to intercalate into the interfaces between Gr or h-BN and SiC, Ru, Cu, Ir and Pt substrates to achieve quasi-free-standing Gr [36].

More intriguingly, the nanospaces between 2D layers and their substrates have also been exploited to catalyze the growth of a 2D thin film. The bilayer growth of Gr on Cu foils was realized by an oxygen-activated CVD process [37, 38], wherein the 2nd Gr layer predominantly grew below the 1st layer, as evidenced by a carbon isotope labeling technique [39]. In addition, the growth of monolayer

Address correspondence to yanfengzhang@pku.edu.cn

h-BN or Gr was also realized in the confined space between non-epitaxial monolayer h-BN and a Ni (111) substrate due to their weak interfacial interaction [40]. Apart from Gr and h-BN, a two-atom-thick GaN layer was also synthesized at the interface of epitaxial Gr and a SiC substrate through a migration-enhanced encapsulated growth mode, in which Ga atoms released by the trimethylgallium precursor, migrated into the interface and reacted with ammonia to form a 2D GaN layer [41]. Briefly, the direct fabrication of heterostructures or bilayer films can be realized through the growth of a second layer inside the confined space between a 2D layer and its substrate. However, the space-confined growth of monolayer TMDCs under 2D materials on specific substrates remains unrealized.

Herein, we present the direct synthesis of an unusual Gr/$ReSe_2$ stack on Au foils through a two-step ambient-pressure CVD (APCVD) route by exploiting the underlayer growth of monolayer $ReSe_2$ below the first-deposited Gr. This abnormal growth behavior was thoroughly examined by various surface/interface characterization methods, including X-ray photoelectron spectroscopy (XPS), scanning Kelvin probe force microscopy (SKPFM), etc. Particularly, the manipulation function of scanning tunneling microscopy (STM) was also utilized to "scratch off" the upper Gr layer and expose the lower $ReSe_2$ layer, so as to confirm the stacking geometry. Moreover, the reaction or intercalation mechanism of monolayer $ReSe_2$ at the vdW gap of Gr/Au was also confirmed by combining experimental results with density functional theory (DFT) calculations. Our work should offer an intriguing strategy for the direct synthesis of 2D heterostructures, and also provide an in-depth understanding of the inherent mechanism of the spaced-confined growth strategy.

2 Results and discussion

The respective growth of monolayer $ReSe_2$ and Gr directly on Au foils by APCVD approaches has been previously reported by our group [42, 43]. On the basis of these results, a direct two-step APCVD route was designed to directly prepare Gr/$ReSe_2$ vertical stacks on Au foils, as schematically shown in Fig. 1(a). In the first step, a nearly full-coverage, highly uniform Gr monolayer was grown on Au foils by the APCVD method, as confirmed by XPS, scanning electron microscopy (SEM), Raman spectroscopy, and atomic force microscopy (AFM) (Figs. S1 and S2 in the Electronic Supplementary Material (ESM)). The monolayer Gr/Au foil sample was then employed as a platform for the synthesis of $ReSe_2$ inside the same CVD furnace. Notably, after the second growth step, well-defined $ReSe_2$ parallelograms (with a long-edge length of ~ 2 μm) can be noticed to present darker contrasts than the Gr layer, according to the SEM images shown in Figs. 1(b) and 1(c). A nearly full-coverage $ReSe_2$ was also obtained by decreasing the precursor–substrate distance (D) from ~ 3 to ~ 1 cm (Fig. 1(d)). The coexistence of Gr and $ReSe_2$ was clearly demonstrated by the XPS data (Fig. S3 in the ESM).

To analyze the stacking behavior, the as-grown sample was then transferred onto SiO_2/Si substrates for further characterizations. According to the corresponding SEM image (Fig. 1(e)), the shape and coverage of $ReSe_2$ are almost identical to those in the as-grown sample. Moreover, some Gr wrinkles also appear to span over the $ReSe_2$ flakes and extend to the neighboring Gr region. These wrinkles possibly arise from the transfer process, providing indirect evidence for the stacking of Gr and $ReSe_2$. Further analysis of the AFM image and corresponding height profile (Fig. S4 in the ESM) address the monolayer nature of the $ReSe_2$ film, which is ~ 0.90 nm in height with respect to the Gr layer. In addition, the whole stacked region shows an apparent height of ~ 1.45 nm with regard to the SiO_2/Si substrate, indicating the formation of Gr/$ReSe_2$ stacks according to the published reports regarding the apparent heights of monolayer Gr (~ 0.7 nm) and $ReSe_2$ (~ 0.9 nm) on SiO_2 [16, 43].

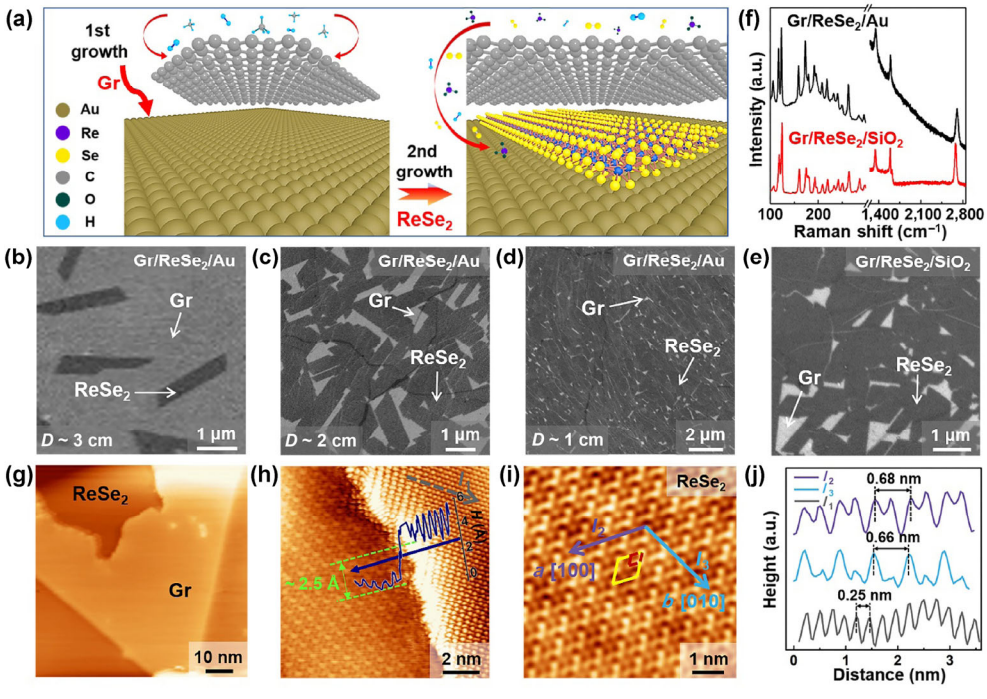

Figure 1 The two-step APCVD synthesis of Gr/$ReSe_2$ vertical stacks on Au foils through a space-confined route and their characterizations. (a) Schematic illustration of the two-step APCVD growth route. (b)–(d) SEM images of as-grown $ReSe_2$ with coverages of ~16%, ~83%, and ~96%, respectively, achieved by varying the precursor–substrate distances (D) from ~ 3.0 to 2.0 and 1.0 cm (synthesized at 750 °C for 20 min under 50 sccm Ar and 5 sccm H_2). The first deposited Gr has a coverage of ~ 100%. (e) SEM image of the Gr/$ReSe_2$ stacks (with D ~ 2.0 cm) transferred onto SiO_2/Si. (f) Comparison of the Raman spectra for as-grown and transferred stacks. (g) Large-scale STM image (–0.01 V, 3.00 nA, 77 nm × 77 nm) of the as-grown sample with coexisting $ReSe_2$ and Gr regions. (h) Atomically-resolved STM image (–0.05 V, 5.00 nA; 11.4 nm × 11.4 nm) of the boundary between the lower $ReSe_2$ and the upper Gr layers. The inset height profile shows a height difference of ~ 2.5 Å from Gr to the $ReSe_2$ region. (i) Atomically-resolved STM image (–0.003 V, 5.71 nA, 6.1 nm × 6.1 nm) of the perfect atomic lattice of $ReSe_2$. The extended unit cell and the top four nonidentical Se atoms in $ReSe_2$ are marked by yellow and red parallelograms, respectively. (j) Corresponding line profiles along the arrows in (h) and (i) showing the different lattice constants of Gr and $ReSe_2$.

Due to the low crystal symmetry of $ReSe_2$, more than 10 distinctive Raman modes occur in the range of 100–300 cm^{-1} for the stacked region (Fig. 1(f) and Fig. S5(a) in the ESM). Among these, two typical Raman peaks located at ~ 123.1 (E_g-like) and ~ 173.1 cm^{-1} (A_g-like) can be observed for the as-grown sample on Au foils, corresponding to the in-plane and out-of-plane vibrational modes of $ReSe_2$, respectively. Notably, the Raman signal of Gr is also visible in the $ReSe_2$ region (Fig. 1(f)), again verifying the formation of Gr and $ReSe_2$ stacks directly on Au foils. Surprisingly, after transfering onto SiO_2/Si, the E_g- and A_g-like vibrational modes of $ReSe_2$ move to ~ 124.5 and ~ 174.8 cm^{-1}, respectively (Fig. 1(f) and Fig. S5(a) in the ESM), corresponding to blueshifts of ~ 1.4 and ~ 1.7 cm^{-1} with respect to that observed for the as-grown stack. Similarly, clear blueshifts in the E_g- and A_g-like peaks of $ReSe_2/SiO_2$ with respect to those of $ReSe_2$/Au were also observed, owing to a weakened adlayer-substrate interaction [43]. However, this fact is apparently different from that of the monolayer MoS_2/Gr system, where no obvious shifts in the E^1_{2g} and A_{1g} peaks of $MoS_2/Gr/SiO_2$ were detected relative to MoS_2/Gr/Au, possibly due to the interfacial screening effect of Gr [16]. Accordingly, the Raman data provide clues for the growth of a $ReSe_2$ layer below Gr on Au foils. To address this premise further, comparative Raman spectra of Gr, Gr/$ReSe_2$ (one-step transfer), $ReSe_2$/Gr (two-step transfer), and Gr/$ReSe_2$ (two-step transfer) on SiO_2/Si substrates are shown in Fig. S5(b) in the ESM to reconfirm the stacking feature of Gr/$ReSe_2$ on Au foils.

STM characterizations were then performed on the vertical stack to show the atomic-scale morphology. To remove the adsorbed contaminants through the maintenance in air, the CVD-grown Gr/$ReSe_2$ on Au foils was degassed at 400 °C for 9 h in an ultrahigh vacuum chamber before the STM measurements. A typical large-scale topographic STM image is displayed in Fig. 1(g). The corresponding atomic-resolution STM image (Fig. 1(h)) presents the coexistence of $ReSe_2$ (on the left) and Gr (on the right) on the same terrace with a height difference of ~ 2.5 Å from Gr to $ReSe_2$ regions. This height difference is similar to the monolayer thickness of Gr. Moreover, a scattering pattern exists near the edge of Gr, displaying a larger lattice ~ 0.43 nm, in agreement with the $\sqrt{3}\times\sqrt{3}$ R30° interference pattern mediated by the scattering of electrons at the domain edge of Gr [42, 44]. The Gr layer is thus inferred to be positioned above the $ReSe_2$ layer.

From the atomically-resolved STM image shown in Fig. 1(i), an extended unit cell for $ReSe_2$ can be identified from the four brightest spots (in line with the uppermost Se atoms), and a smaller unit cell can also be achieved by the four adjacent spots with gradually increased contrasts, consistent with four nonidentical adjacent Se atoms. These two type unit cells are respectively marked by yellow and red parallelograms. Notably, the "yellow" unit cell size is double of the "red" one due to the breakage of hexagonal symmetry in the distorted 1T structure [45, 46]. Herein, the four Se atoms highlighted by the red parallelogram exhibit various STM contrasts, which is either because these four Se atoms are not located in the same plane [47, 48] or because they contribute differently to the density of states (DOS) [47, 49]. The *b* and *a* axes marked in Fig. 1(i) represent the directions of the shortest and second-shortest lattice constants, respectively, and the *b* axis is aligned with the one-dimensional (1D) atomic chain direction of the Re atoms [50–52]. According to the line profile analyses in Fig. 1(j), the periods along the *a* and *b* axes are ~ 0.68 and ~ 0.66 nm, respectively, consistent with the previous report for $ReSe_2$ [51]. Besides, the height profile (bottom of Fig. 1(j)) taken along the gray arrow labeled I_1 in Fig. 1(h) manifests a lattice constant of ~ 0.25 nm, fully consistent with the lattice parameter of Gr. In this regard, the atomically resolved STM observations can be utilized to identify the coexisting Gr and $ReSe_2$ regions on Au foils.

To uncover the interface growth mechanism of $ReSe_2$ at monolayer Gr/Au, an incomplete monolayer Gr was synthesized on Au foils, serving as a platform for the second growth stage, as shown in Figs. 2(a)–2(c) for 5 minute-growth. Although imaged randomly by SEM (Figs. 2(a) and 2(b)), the common feature is that Gr edges and grain boundaries are highlighted by $ReSe_2$ flakes. That means, the initially evolved $ReSe_2$ domains on Au may extend several microns and dive into the interface of Gr/Au, when their growth fronts encounter with some graphene domains, as shown in the close-up image in Fig. 2(c). The stacked regions usually show darker contrasts than that of pure $ReSe_2$ on Au regions, due to the covering of a Gr layer. Intriguingly, some quadrilateral shape islands can be noticed to evolve on Au but with some regions trapped inside the edge of Gr/Au. Intriguingly, the quadrilateral island shape can be perfectly maintained even underneath the Gr layer, suggesting the similar growth behavior of $ReSe_2$ on Au and at the interface of Gr/Au.

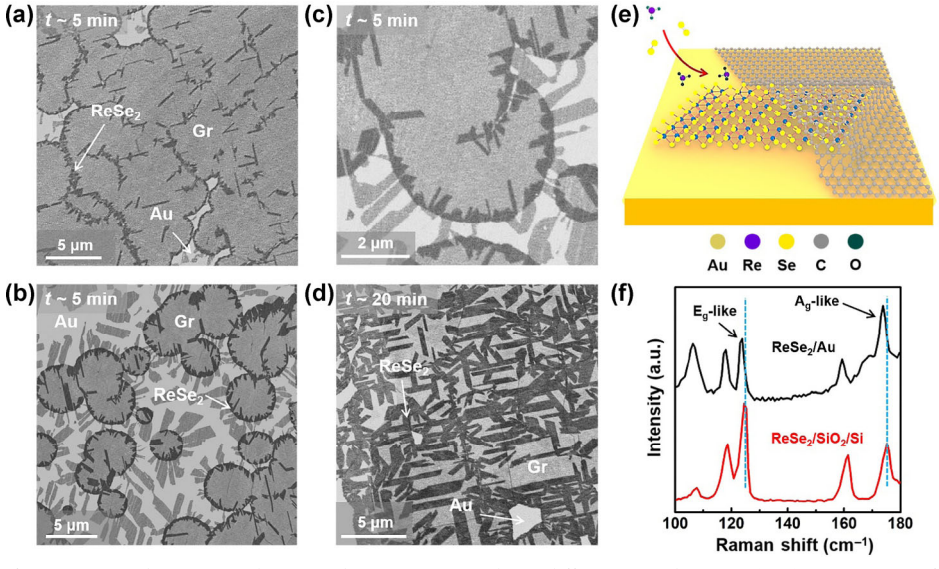

Figure 2 Characterizations for $ReSe_2$ growth on incomplete monolayer Gr/Au samples at different growth time. (a)–(c) SEM images of $ReSe_2$ growth on incomplete Gr/Au for 5 min, revealing the unique growth behavior of monolayer $ReSe_2$ growing from the Au surface into the interface of monolayer Gr/Au through the domain boundary/edge of Gr (showing darker contrasts than Gr). (d) SEM image of $ReSe_2$ growth on incomplete Gr/Au for 20 min showing increased $ReSe_2$ coverage. (e) Schematic illustration showing the growth of $ReSe_2$ into the interface of Gr/Au from the domain boundary/edge of the incomplete Gr layer. (f) Comparative Raman spectra for as-grown $ReSe_2$ on Au foils and transferred on SiO_2/Si, suggesting the relative strong interface interaction of $ReSe_2$/Au.

However, after 20 min growth (Fig. 2(d)), larger $ReSe_2$ domains tend to evolve with the a more uniform quadrilateral shape. To explain this unique growth behavior, the interface interaction between $ReSe_2$ with Au is intensively explored with Raman spectroscopy. Notably, simultaneous blue shifts of the E_g- and A_g-like vibrational modes from ~ 123.5 and ~ 173.8 to ~ 124.5 and ~ 175.1 cm^{-1} can be noticed on the transferred $ReSe_2$ on SiO_2/Si with regard to that on Au foils (Fig. 2(f)), possibly mediated by the weakened adlayer–substrate interaction [43]. This case also happened to as-grown and transferred Gr/$ReSe_2$ stacks (see Fig. 1(f) and Fig. S5(a) in the ESM). In this regard, the stronger interaction between $ReSe_2$ and Au with regard to that of Gr/Au should be the driving force for the interface confined growth behavior, as schematically illustrated in Fig. 2(e).

High-angle annular dark-field scanning transmission electron microscopy (HAADF-STEM) was also employed to characterize the stacked Gr and $ReSe_2$ stacks. Notably, the low-magnification transmission electron microscopy (TEM) image (Fig. 3(a)) shows a significant different contrast for Gr and $ReSe_2$ regions, mainly owing to their different atomic numbers (C and Re). Moreover, the selected-area electron diffraction (SAED) pattern (inset of Fig. 3(a)) of the stacked region presents two sets of diffraction spots corresponding to Gr and $ReSe_2$ (~ 0.25 and ~ 0.33 nm in lattice constants, respectively), and a relative rotation angle of ~ 8°. The unique distorted structure is also confirmed by a HAADF-STEM image (Fig. 3(b)) showing both Re and Se atoms forming a unique 1T phase. Notably, almost no defects are visible in the TEM images, suggesting a rather high crystalline quality of the confined $ReSe_2$ flake. This TEM result hereby provides an additional proof for the proposed vertical stacking geometry of Gr/$ReSe_2$ on Au foils.

Comparative microscopic/spectroscopic investigations were also performed to confirm the vertical stacking geometry. SKPFM has been proven to be effective for evaluating the stacking geometries of WS_2/MoS_2, MoS_2/WS_2, and Gr/h-BN via comparison of their local electrical properties or surface potentials [53, 54]. Herein, the surface potential distribution of a Gr/$ReSe_2$ vertical stack transferred onto SiO_2/Si (from Au foils) was obtained and compared with an inverted stack obtained by transferring monolayer CVD-$ReSe_2$ onto Gr/SiO_2 (Figs. 3(d)and 3(f)). The corresponding AFM images are presented in Figs. 3(c) and 3(e), respectively, with Gr fully covered on the surface and $ReSe_2$ possessing a sublayer coverage. Notably, almost no obvious contrast/potential difference can be noticed in the SKPFM image of the Gr/$ReSe_2$ stack (Fig. 3(d)), while an ~ 88 meV surface potential difference can be defined between Gr and $ReSe_2$ in the inverted $ReSe_2$/Gr stack (Fig. 3(f)). This result verifies the stacking geometry of Gr/$ReSe_2$/Au foils synthesized in this work since the coated Gr layer gives a homogenous surface potential distribution. More AFM and SKPFM data are supplied in Fig. S6 in the ESM to further confirm the current prediction.

Furthermore, XPS depth analysis was also carried out on the as-grown Gr/$ReSe_2$ sample on Au foil. As shown in Fig. 3(g), the concentration of C dramatically decreased with increasing etching time (below 42 s), while the concentrations of Re and Se gradually increased. More importantly, when the concentration of C decreased to ~ 1% at an etching time of 72 s, the concentration of Re and Se still maintained at ~ 30%. These data further support the fact that the secondly deposited $ReSe_2$ is located underneath the Gr layer. Additionally, according to the XPS analysis shown in Fig. 3(h), the as-grown Gr/Au sample exhibits a characteristic C 1s peak located at 284.33 eV, while the value for as-grown Gr/$ReSe_2$/Au is 284.16 eV. According to the published report, this shift to a lower binding energy indicates the presence of a weaker Gr and metal interaction [55–57], suggesting the formation of Gr/$ReSe_2$ rather than $ReSe_2$/Gr on Au foils. More detailed XPS analysis is supplied in Figs. S7 and S8 in the ESM.

STM has also been widely used in the modification/construction of nanomaterials by virtue of the interactions between STM tip and sample surfaces [58-60]. And the tip-sample interaction is ascribed to electrostatic and chemical forces, which can induce a strong electric field between the STM tip and the sample surface [58]. As reported before, Gr can be scraped off from the graphite surface using STM by applying a voltage ramp at the edge of a terrace and then scanning perpendicular to the edge [58]. In this work, STM was also utilized to directly visualize the stacking geometry of Gr and $ReSe_2$ by scraping off the upper Gr layer and exposing the lower $ReSe_2$. The "cutting open" and subsequent "scraping off" processes are schematically illustrated in Fig. 4(a). A bias voltage applied

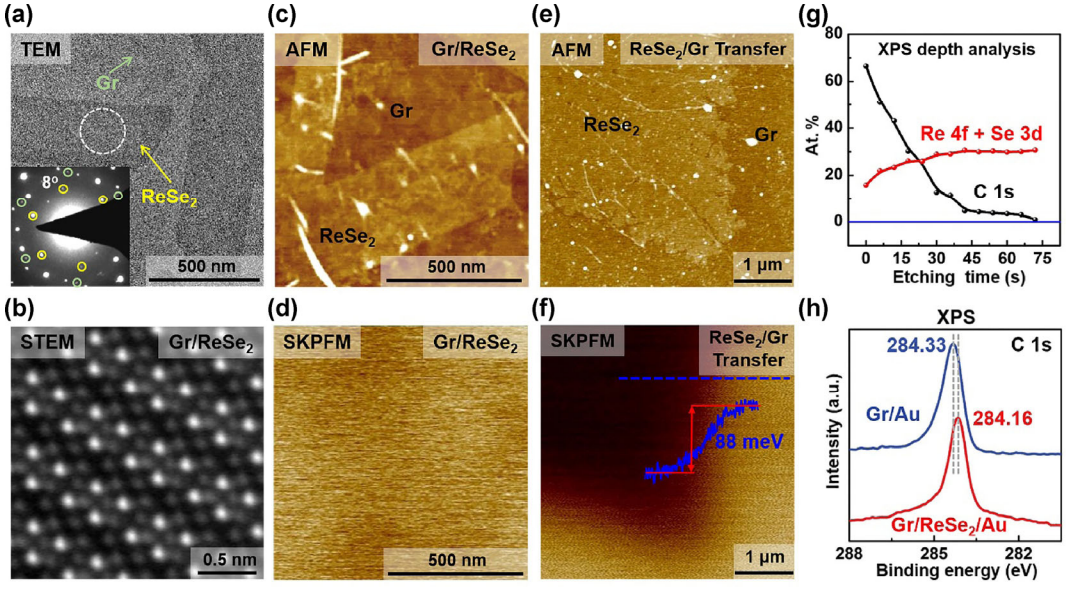

Figure 3 Verification of the vertical stacking geometry of Gr/$ReSe_2$/Au foil by comparative microscopic/spectroscopic characterizations. (a) Low-magnification TEM image of the transferred Gr/$ReSe_2$ vertical stack. Inset: corresponding SAED pattern collected from the circled area displaying two sets of diffraction spots from both Gr and $ReSe_2$ with a rotation angle of ~ 8°. (b) Z-contrast STEM image resolving the atomic arrangement of a single layer $ReSe_2$ underneath a Gr cover. (c) and (d) AFM and SKPFM surface potential images, respectively, of the Gr/$ReSe_2$ vertical stack (from Au foils) transferred onto SiO_2/Si. (e) and (f) AFM and SKPFM surface potential images, respectively, of an inverted stack achieved by transferring monolayer $ReSe_2$ onto Gr/SiO_2/Si. (g) Atomic concentrations of C (black spheres) and Re with Se (red spheres) as a function of etching time obtained from XPS depth analysis. (h) C 1s XPS spectra of as-grown Gr/Au foil (blue line) and as-grown Gr/$ReSe_2$/Au foil (red line) showing the change in the binding energy of C 1s from 284.33 to 284.16 eV.

between the sample surface and STM tip can induce charges and electrostatic attraction between them. This attraction force weakens the coupling between Gr and the rest of the platform, allowing it to be "scraped off". Practically, sequential time-dependent STM images were captured (Figs. 4(b)–4(d)) to display the detailed process.

In Fig. 4(b), a "void region" occurs at the grain boundary (GB) of Gr, leading to the exposure of the underneath $ReSe_2$ layer, as confirmed by the atomic-resolution STM image shown in Fig. 4(f) (magnification of the marked region in Fig. 4(b)). Intriguingly, through 5-hour STM scanning, the exposed $ReSe_2$ region expands gradually, along with the "scraped off" of the Gr coating, as shown in Figs. 4(c) and 4(d) (after scanning for 2 and 5 h). The phenomenon can be supported by several facts. First, the broken Gr island "floats" on a $ReSe_2$ layer, as defined by the different contrasts and apparent heights of Gr and $ReSe_2$ (Fig. 4(h)). Second, the edge of the Gr island presents an irregular shape and shows brighter contrast at the crooked edges, which is possibly due to the unstable binding of the edges to the underneath $ReSe_2$ layer. Third, the $ReSe_2$ lattice underneath possesses the same lattice orientation around the edges of upper Gr layer, i.e., the underneath $ReSe_2$ layer is continuous over the scanned area. More scanning-time-dependent STM images are supplied in Fig. S9 in the ESM, revealing the "scraping off" of even larger Gr regions and the exposure of a larger $ReSe_2$ film. Notably, some clusters and fragments (as shown in Fig. S9(g) in the ESM) appear on the newly exposed $ReSe_2$ regions after scrapping off the upper Gr layer, which are proposed to be the residues of the scratched Gr. These fragments tend to exhibit an amorphous state with low crystallinity, instead of intact Gr patches with honeycomb lattices (Fig. S9(h) in the ESM). Briefly, these sequential STM observations provide direct proof of the proposed Gr/$ReSe_2$ stacking geometry.

Notably, a more detailed structure (or STM contrast) of the upper Gr layer can also be obtained by high-resolution STM imaging, which is also useful for identifying the stacking geometry of Gr/$ReSe_2$. First, as a reference, Fig. 4(f) displays the atomically-resolved STM image of monolayer $ReSe_2$ on Au(111), which presents a moiré superstructure induced by the lattice mismatch between $ReSe_2$ and Au(111) (a_{ReSe2} = 0.332 nm, $a_{Au(111)}$ = 0.288 nm). The periods along the two directions are A = 2.33 ± 0.01 nm and B = 2.00 ± 0.01 nm, and the intersection angle is ~ 60°, approximately corresponding to a (7 × 6) $ReSe_2$ on an (8 × 7) Au(111) supercell. This anisotropic moiré period similarly originates from the anisotropy of the distorted 1T structure of $ReSe_2$. A simulation was also performed by rotating the $ReSe_2$ lattice by ~ 4° with respect to Au(111), as schematically shown in Fig. 4(e).

Notably, the moiré structure of Gr around the exposed $ReSe_2$ region exhibits almost an identical moiré period with that of $ReSe_2$, as outlined by the parallelogram in Fig. 4(g), where A' = 2.31 ± 0.03 nm and B' = 2.00 ± 0.01 nm. However, the surface undulation/contrast is smaller than that of $ReSe_2$ on Au(111). In addition, the two sets of fast Fourier transform (FFT) spots observed for the two moiré structures are completely coincident, as highlighted by the white squares in the insets of Figs. 4(f) and 4(g). This result indicates that, the moiré patterns on both $ReSe_2$/Au(111) and Gr/$ReSe_2$/Au(111) present the same period. This period cannot originate from the lattice mismatch of Gr/$ReSe_2$ since the possible maximum value between them is calculated to be ~ 1.21 nm (Fig. S10(a) in the ESM), much smaller than the current case ~ 2 nm. Hence, the moiré modulation from $ReSe_2$/Au(111) is proposed to penetrate through the upper Gr layer and imaged by STM for the Gr/$ReSe_2$/Au(111). This resembles the semitransparency effect of Gr monolayer on SiC [61], GaAs(110) and InAs(110) [62], where the atomic structure of substrate can be imaged by STM through the upper Gr layer. However, the moiré modulation can only be observed at high sample biases since the substrate orbitals are positioned above and below the E_f, while the Gr states exist within the bandgap of substrate [61]. In contrast, the moiré pattern from the $ReSe_2$/Au(111) system is bias-independent, similar to the semitransparency feature of Gr on clean Si(100), which is attributed to the stronger interface interaction between Gr and substrate [63]. The stacking geometry is thus inferred to be Gr/$ReSe_2$/Au(111) for the regions with a moiré period of ~ 2 nm but with a less intense STM contrast. For more proof, statistical analysis of the moiré periods (the second longest one, like B' in Figs. 4(f) and 4(g)) in various regions was also performed and showed a narrow range of 1.9–2.2 nm, in line with a small relative rotation of 4°–6° between $ReSe_2$ and Au(111) in Gr/$ReSe_2$/Au, as displayed in Fig. S10(b) in the ESM.

As reported before, some metals (such as Cs, Pb, Ge, and alkali

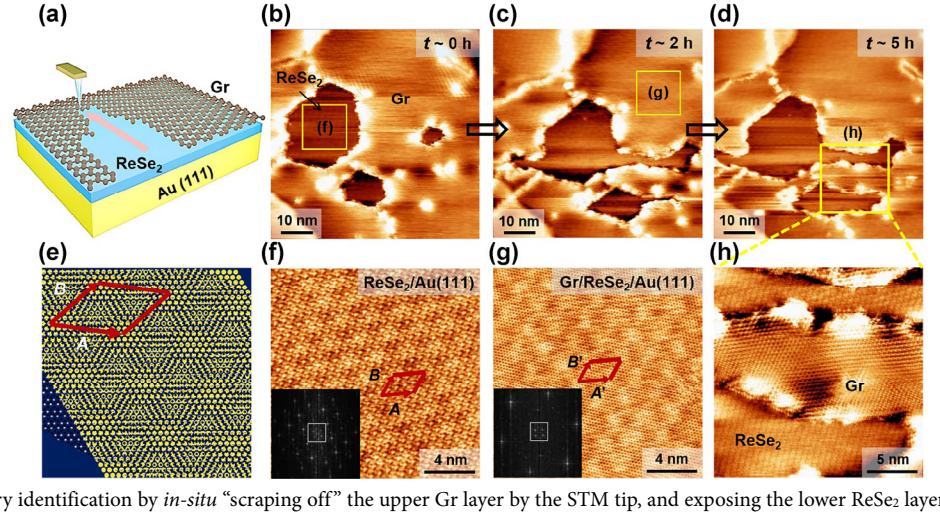

Figure 4 Stacking geometry identification by *in-situ* "scraping off" the upper Gr layer by the STM tip, and exposing the lower $ReSe_2$ layer on the Au(111) facet of Au foils. (a) Schematic of the scraping process for removing the upper Gr layer through long-time STM scanning. (b)–(d) Scanning-time-dependent STM images showing the scraping progress after 0, 2 and 5 h of scanning, respectively (–0.04 V, 4.29 nA; 65.5 nm × 65.5 nm). (e) Schematic illustration of the moiré pattern formed for a 1.41°-rotated $ReSe_2$ lattice with respect to Au(111), with the moiré unit marked by a red parallelogram. Black and white spheres represent Se and Re atoms, respectively, while Au atoms are shown in yellow. (f) and (g) Magnified STM images (–0.003 V, 16.83 nA; –0.004 V, 8.36 nA; 16.4 nm × 16.4 nm) of the yellow square regions marked in (b) and (c) typical for $ReSe_2$ and Gr, respectively. The unit cell of the moiré pattern is marked by a red parallelogram. Insets: corresponding 2D FFT patterns showing the coexistence of the moiré pattern (marked with a white square) and the atomic lattice. The moiré periods on $ReSe_2$/Au(111) (f) and Gr/$ReSe_2$/Au(111) (g) are exactly the same but with different undulations. (h) Magnified STM image (–0.007 V, 2.42 nA; 20.5 nm × 20.5 nm) of the region marked by the yellow square in (d) exposing the upper Gr and the lower $ReSe_2$.

metals), and molecules (such as O_2 and CO) complied with the defect-aided mechanism in intercalating into the interfaces between Gr and substrates [26, 31, 64–67]. And the intercalation channels were proven to be the extended defects, such as the GBs, point defects and island edges [55]. Herein, the Gr GBs, edges, and void defects are expected to serve as pathways for the penetration of the Re- and Se-related precursors into the Gr/Au foil interface, further promoting the growth of monolayer $ReSe_2$ under the Gr layer, as schematically illustrated in Figs. 5(c) and 5(d).

Figure 5(a) displays a large-scale STM image of the Gr/$ReSe_2$/Au sample. On the same Au terrace, the void regions (in line with the exposed $ReSe_2$ areas) are mainly located at the GB of Gr, presenting darker contrast than the neighboring Gr region, as evidenced by the atomic-resolution image in Fig. 5(b). Additional STM images of the Gr boundary are provided in Fig. S11 in the ESM. In this regard, the domain boundary is expected to serve as a channel for the intercalation of the reactive precursors. This fact is also reflected by the large-scale SEM observations obtained during the initial growth of $ReSe_2$ (Figs. 2(a) and 2(b)). The accumulated $ReSe_2$ at edges and GBs is proposed to decouple the interaction between the boundary/edge of Gr and the substrate, driving the further intercalation of precursors, as similarly reported for the growth of monolayer GaN under Gr [41]. Occasionally, these void regions also appear inside the Gr domains along with the exposure of the underlying $ReSe_2$ (Fig. S12 in the ESM). Moreover, some $ReSe_2$ flakes tend to aggregate around wrinkles of Gr at the initial growth of $ReSe_2$ (Fig. S13 in the ESM), which indicates that the nanoscale tears at apex of wrinkles may also serve as the penetration pathways for precursors [41]. Briefly, GBs and defects should serve as channels for the penetration of the active Re and Se precursors into the Gr/Au interface, and ultimately facilitate the growth of a $ReSe_2$ monolayer.

To determine the intercalation-induced growth mechanism of Gr/$ReSe_2$/Au, the adsorption energies of a single Re atom, a single Se atom and a ReSe cluster on the free surface of Au(111), at the interface between Gr and Au, and both under and above the Gr layer were calculated by using first-principles calculations within DFT. Figure 5(e) reveals the adsorption energies of the considered atoms and clusters at the different adsorption sites. Notably, the Se atom prefers to bind to Re or to the unsaturated Gr edge (e.g., GBs of Gr, right panel of Fig. 5(f)) marked with the thicker orange rod, while the other atom and cluster tend to directly adsorb at the interface, as shown in Fig. 5(f) for the most stable configurations. Moreover, the adsorption energies of Re, Se, ReSe are much higher above Gr than under it. For example, the adsorption energy of Re on Gr is as high as 4.6 eV, whereas a value ~ 0.35 eV is resulted with Re positioned underneath Gr. Accordingly, $ReSe_2$ prefers to grow within the confined space of Gr/Au, which is in contrast with the two-step CVD-grown MoS_2/Gr/Au [16, 68].

3 Conclusion

In summary, we have detected a novel confined growth behavior of monolayer $ReSe_2$ in the vdW gap of the first-grown Gr and its Au substrate by employing a two-step APCVD method. The unique stacking geometry of Gr/$ReSe_2$/Au foils is unambiguously verified by scraping off the upper Gr layer with STM and exposing the lower $ReSe_2$. The domain boundaries and edge sites are proposed to act as channels for the intercalation of Re and Se precursors into the Gr/Au foil interface, thus facilitating the growth of $ReSe_2$. This work hereby presents the first demonstration that, a semiconducting TMDC layer can be synthesized at a confined reactor composed of a 2D layer and its substrate, thus offering an intriguing strategy for obtaining high-quality 2D-stacked heterostructures. Exploration of the confined reactions in a nanoreactor is also essential for exploiting the surface or interfacial properties of 2D layered materials.

4 Experimental

4.1 Synthesis of Gr/$ReSe_2$ heterostructures

A full-coverage monolayer Gr film was synthesized on Au foils (Zhong Nuo Advanced Material Technology Co., Ltd., 30 μm thick, 99.99% purity) by APCVD with CH_4 (1.5 sccm), H_2 (30 sccm), and Ar (200 sccm) carrier gases at 970 °C. $ReSe_2$ was grown by the same APCVD route with ReO_3 (Alfa Aesar, purity 99.9%) and Se (Alfa Aesar, purity 99+%) as precursors. All the sample growth processes were completed in a multi-temperature-zone furnace equipped with a quartz tube (1 inch in diameter). In the second growth step, the

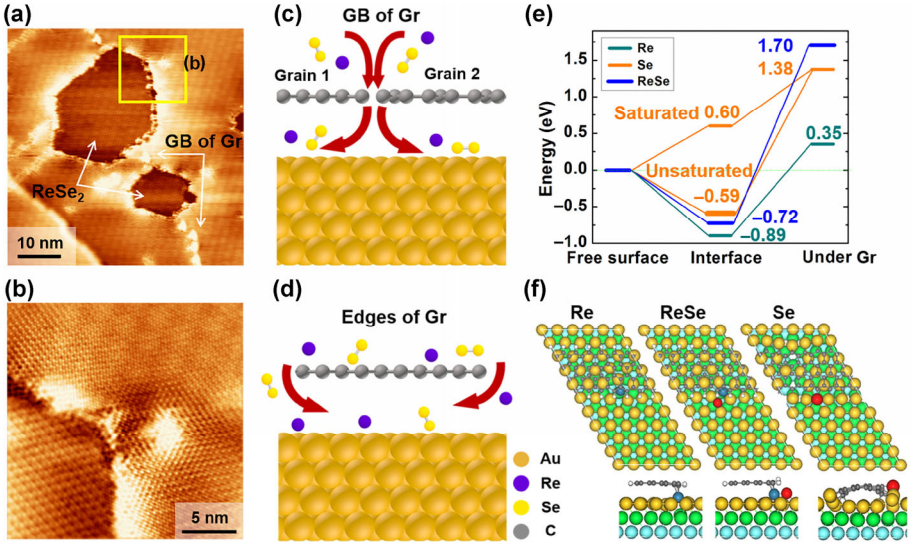

Figure 5 The intercalation mechanism and pathways for the growth of $ReSe_2$ underneath Gr on Au foils. (a) Large-scale STM image (–0.018 V, 6.77 nA; 55 nm × 55 nm) of Gr/$ReSe_2$/Au foils showing the formation of "void regions" at the domain boundaries of Gr. (b) Magnified STM image (–0.005 V, 2.64 nA; 16.38 nm × 16.38 nm) of the yellow square region in (a). (c) and (d) Schematics of the proposed pathways for the intercalation of Re and Se atoms through the Gr GBs and edges, respectively. (e) Adsorption energy diagram of the different adsorption sites (on the Au(111) free surface, at the interface between Gr and Au, under Gr) for Re, Se and ReSe. The Gr/Au(111) interface is more likely than the other sites to trap Re and Se due to its relatively lower adsorption energies. (f) Top and side views of the most stable adsorption geometries of Re, ReSe and Se on the Au(111) facet. Blue and red spheres represent Re and Se atoms, respectively, while the Au atoms in the different layers are sequentially colored in orange, green and cyan.

typical temperatures of Gr/Au, ReO_3 and Se powders were 750, 750 and 250 °C, respectively. Ar (50 sccm) and H_2 (5 sccm) were utilized as the carrier gases. After growth, the Gr/$ReSe_2$ stacks were detached from Au foils and transferred onto target substrates using the electrochemical bubbling method.

4.2 Characterizations

The samples were systematically characterized using SEM (Hitachi S-4800, 2 kV), commercial multifunction AFM (Bruker Dimension Icon), Raman spectroscopy (HORIBA iHR550, excitation light of 532 nm wavelength), XPS (Kratos Analytical AXIS-Ultra with monochromatic Al Kα X-rays), TEM (FEI Tecnai F20, acceleration voltage of 200 kV). STEM was performed at an aberration-corrected FEI Titan Cubed Themis G2 at 300 kV with a beam current of 60 pA, a convergence semi-angle of 21.5 mrad, and a collection semi-angle snap in the range of 80–379 mrad. STM characterization was performed by utilizing an Omicron ultrahigh vacuum variable temperature scanning tunneling microscope under a base pressure better than 1×10^{-8} mbar.

4.3 DFT calculations

All calculations were performed with the Vienna *ab-initio* simulation package [69], adopting Perdew–Burke–Ernzerhof (PBE) [70] approximation to the exchange-correlation effect. The projector-augmented wave potentials [71, 72] were selected to describe the ion-electron interaction. To simulate the Gr–Au interface, a 5 × 10 Au(111) surface was chosen as the substrate, on which Gr nanoribbons with four zigzag chains in the width direction and six unit cells along the periodic direction were adsorbed. With this setting, the strain introduced in Gr nanoribbons is less than 1%. To account for the weak vdW interaction, the Tkatchenko-Scheffler method [73] was applied. All structures were relaxed until the force on each atom was smaller than 0.02 eV/Å.

Acknowledgements

This work was supported by the National Natural Science Foundation of China (Nos. 51472008, 51861135201, 51290272, 61774003, 51502007, and 51672007), the National Key Research and Development Program of China (Nos. 2016YFA0200103, 2017YFA0205700, and 2017YFA0304600), the Open Research Fund Program of the State Key Laboratory of Low-Dimensional Quantum Physics (Nos. KF201601 and KF201604) and "2011 Program" Peking-Tsinghua-IOP Collaborative Innovation Center of Quantum Matter. The authors acknowledge Electron Microscopy Laboratory in Peking University for the use of Cs corrected electron microscope. The theoretical simulations of this work were supported by the Youth 1000-Talent Program of China, the Shenzhen Basic Research Project (No. JCYJ20170407155608882), and the Development and Reform Commission of Shenzhen Municipality for the development of the "Low-Dimensional Materials and Devices" Discipline. The computations were carried out at National Supercomputer Center in Tianjin, and the calculations were performed on TianHe-1 (A).

Electronic Supplementary Material: Supplementary material (further details of XPS spectrum, Raman spectroscopy measurements, STM measurements, AFM imaging, SKPFM images, and SEM images) is available in the online version of this article at https://doi.org/10.1007/s12274-018-2194-6.

References

[1] Offidani, M.; Milletarì, M.; Raimondi, R.; Ferreira, A. Optimal charge-to-spin conversion in graphene on transition-metal dichalcogenides. *Phys. Rev. Lett.* **2017**, *119*, 196801.

[2] Li, W.; Ding, H.; Deng, P.; Chang, K.; Song, C. L.; He, K.; Wang, L. L.; Ma, X. C.; Hu, J. P.; Chen, X. et al. Phase separation and magnetic order in K-doped iron selenide superconductor. *Nat. Phys.* **2011**, *8*, 126–130.

[3] Georgiou, T.; Jalil, R.; Belle, B. D.; Britnell, L.; Gorbachev, R. V.; Morozov, S. V.; Kim, Y. J.; Gholinia, A.; Haigh, S. J.; Makarovsky, O. et al. Vertical field-effect transistor based on graphene-WS_2 heterostructures for flexible and transparent electronics. *Nat. Nanotechnol.* **2013**, *8*, 100–103.

[4] Tang, H. L.; Chiu, M. H.; Tseng, C. C.; Yang, S. H.; Hou, K. J.; Wei, S. Y.; Huang, J. K.; Lin, Y. F.; Lien, C. H.; Li, L. J. Multilayer graphene–WSe_2 heterostructures for WSe_2 transistors. *ACS Nano* **2017**, *11*, 12817–12823.

[5] Yu, L. L.; Lee, Y. H.; Ling, X.; Santos, E. J. G.; Shin, Y. C.; Lin, Y. X.; Dubey, M.; Kaxiras, E.; Kong, J.; Wang, H. et al. Graphene/MoS_2 hybrid technology for large-scale two-dimensional electronics. *Nano Lett.* **2014**, *14*, 3055–3063.

[6] Withers, F.; Del Pozo-Zamudio, O.; Mishchenko, A.; Rooney, A. P.; Gholinia, A.; Watanabe, K.; Taniguchi, T.; Haigh, S. J.; Geim, A. K.; Tartakovskii, A. I. et al. Light-emitting diodes by band-structure engineering in van der Waals heterostructures. *Nat. Mater.* **2015**, *14*, 301–306.

[7] Massicotte, M.; Schmidt, P.; Vialla, F.; Schädler, K. G.; Reserbat-Plantey, A.; Watanabe, K.; Taniguchi, T.; Tielrooij, K. J.; Koppens, F. H. L. Picosecond photoresponse in van der Waals heterostructures. *Nat. Nanotechnol.* **2015**, *11*, 42–46.

[8] Zhang, W. J.; Chuu, C. P.; Huang, J. K.; Chen, C. H.; Tsai, M. L.; Chang, Y. H.; Liang, C. T.; Chen, Y. Z.; Chueh, Y. L.; He, J. H. et al. Ultrahigh-gain photodetectors based on atomically thin graphene-MoS_2 heterostructures. *Sci. Rep.* **2014**, *4*, 3826.

[9] Wang, Q. S.; Wen, Y.; He, P.; Yin, L.; Wang, Z. X.; Wang, F.; Xu, K.; Huang, Y.; Wang, F. M.; Jiang, C. et al. High-performance phototransistor of epitaxial PbS nanoplate-graphene heterostructure with edge contact. *Adv. Mater.* **2016**, *28*, 6497–6503.

[10] Deng, D. H.; Novoselov, K. S.; Fu, Q.; Zheng, N. F.; Tian, Z. Q.; Bao, X. H. Catalysis with two-dimensional materials and their heterostructures. *Nat. Nanotechnol.* **2016**, *11*, 218–230.

[11] Haigh, S. J.; Gholinia, A.; Jalil, R.; Romani, S.; Britnell, L.; Elias, D. C.; Novoselov, K. S.; Ponomarenko, L. A.; Geim, A. K.; Gorbachev, R. Cross-sectional imaging of individual layers and buried interfaces of graphene-based heterostructures and superlattices. *Nat. Mater.* **2012**, *11*, 764–767.

[12] Yu, W. J.; Liu, Y.; Zhou, H. L.; Yin, A. X.; Li, Z.; Huang, Y.; Duan, X. F. Highly efficient gate-tunable photocurrent generation in vertical heterostructures of layered materials. *Nat. Nanotechnol.* **2013**, *8*, 952–958.

[13] Tan, C. L.; Zhang, H. Epitaxial growth of hetero-nanostructures based on ultrathin two-dimensional nanosheets. *J. Am. Chem. Soc.* **2015**, *137*, 12162–12174.

[14] Chen, Z. L.; Guan, B. L.; Chen, X. D.; Zeng, Q.; Lin, L.; Wang, R. Y.; Priydarshi, M. K.; Sun, J. Y.; Zhang, Z. P.; Wei, T. B. et al. Fast and uniform growth of graphene glass using confined-flow chemical vapor deposition and its unique applications. *Nano Res.* **2016**, *9*, 3048–3055.

[15] Shi, Y. M.; Zhou, W.; Lu, A. Y.; Fang, W. J.; Lee, Y. H.; Hsu, A. L.; Kim, S. M.; Kim, K. K.; Yang, H. Y.; Li, L. J. et al. Van der Waals epitaxy of MoS_2 layers using graphene as growth templates. *Nano Lett.* **2012**, *12*, 2784–2791.

[16] Shi, J. P.; Liu, M. X.; Wen, J. X.; Ren, X. B.; Zhou, X. B.; Ji, Q. Q.; Ma, D. L.; Zhang, Y.; Jin, C. J.; Chen, H. J. et al. All chemical vapor deposition synthesis and intrinsic bandgap observation of MoS_2/graphene heterostructures. *Adv. Mater.* **2015**, *27*, 7086–7092.

[17] Zhang, Z. P.; Ji, X. J.; Shi, J. P.; Zhou, X. B.; Zhang, S.; Hou, Y.; Qi, Y.; Fang, Q. Y.; Ji, Q. Q.; Zhang, Y. et al. Direct chemical vapor deposition growth and band-gap characterization of MoS_2/h-BN van der Waals heterostructures on Au foils. *ACS Nano* **2017**, *11*, 4328–4336.

[18] Fu, L.; Sun, Y. Y.; Wu, N.; Mendes, R. G.; Chen, L. F.; Xu, Z.; Zhang, T.; Rümmeli, M. H.; Rellinghaus, B.; Pohl, D. et al. Direct growth of MoS_2/h-BN heterostructures via a sulfide-resistant alloy. *ACS Nano* **2016**, *10*, 2063–2070.

[19] Li, G.; Zhou, H. T.; Pan, L. D.; Zhang, Y.; Huang, L.; Xu, W. Y.; Du, S. X.; Ouyang, M.; Ferrari, A. C.; Gao, H. J. Role of cooperative interactions in the intercalation of heteroatoms between graphene and a metal substrate. *J. Am. Chem. Soc.* **2015**, *137*, 7099–7103.

[20] Yan, A. M.; Velasco, J. Jr.; Kahn, S.; Watanabe, K.; Taniguchi, T.; Wang, F.; Crommie, M. F.; Zettl, A. Direct growth of single- and few-layer MoS_2 on h-BN with preferred relative rotation angles. *Nano Lett.* **2015**, *15*, 6324–6331.

[21] Yu, H.; Yang, Z. Z.; Du, L. J.; Zhang, J.; Shi, J. A.; Chen, W.; Chen, P.; Liao, M. Z.; Zhao, J.; Meng, J. L. et al. Precisely aligned monolayer MoS_2 epitaxially grown on h-BN basal plane. *Small* **2017**, *13*, 1603005.

[22] Li, H.; Wu, J. B.; Ran, F. R.; Lin, M. L.; Liu, X. L.; Zhao, Y. Y.; Lu, X.; Xiong, Q. H.; Zhang, J.; Huang, W. et al. Interfacial interactions in van der Waals heterostructures of MoS_2 and graphene. *ACS Nano* **2017**, *11*, 11714–11723.

[23] Varykhalov, A.; Sánchez-Barriga, J.; Shikin, A. M.; Biswas, C.; Vescovo, E.; Rybkin, A.; Marchenko, D.; Rader, O. Electronic and magnetic properties of quasifreestanding graphene on Ni. *Phys. Rev. Lett.* **2008**, *101*, 157601.

[24] Gierz, I.; Suzuki, T.; Weitz, R. T.; Lee, D. S.; Krauss, B.; Riedl, C.; Starke, U.; Höchst, H.; Smet, J. H.; Ast, C. R. et al. Electronic decoupling of an epitaxial graphene monolayer by gold intercalation. *Phys. Rev. B* **2010**, *81*, 235408.

[25] Virojanadara, C.; Watcharinyanon, S.; Zakharov, A. A.; Johansson, L. I. Epitaxial graphene on 6H-SiC and Li intercalation. *Phys. Rev. B* **2010**, *82*, 205402.

[26] Petrović, M.; Šrut Rakić, I.; Runte, S.; Busse, C.; Sadowski, J. T.; Lazić, P.; Pletikosić, I.; Pan, Z. H.; Milun, M.; Pervan, P. et al. The mechanism of caesium intercalation of graphene. *Nat. Commun.* **2013**, *4*, 2772.

[27] Weser, M.; Voloshina, E. N.; Horn, K.; Dedkov, Y. S. Electronic structure and magnetic properties of the graphene/Fe/Ni(111) intercalation-like system. *Phys. Chem. Chem. Phys.* **2011**, *13*, 7534–7539.

[28] Gao, T.; Gao, Y. B.; Chang, C. Z.; Chen, Y. B.; Liu, M. X.; Xie, S. B.; He, K.; Ma, X. C.; Zhang, Y. F.; Liu, Z. F. Atomic-scale morphology and electronic structure of manganese atomic layers underneath epitaxial graphene on SiC(0001). *ACS Nano* **2012**, *6*, 6562–6568.

[29] Zhang, Y.; Zhang, Y. F.; Ma, D. L.; Ji, Q. Q.; Fang, W.; Shi, J. P.; Gao, T.; Liu, M. X.; Gao, Y. B.; Chen, Y. B. et al. Mn atomic layers under inert covers of graphene and hexagonal boron nitride prepared on Rh(111). *Nano Res.* **2013**, *6*, 887–896.

[30] Riedl, C.; Coletti, C.; Iwasaki, T.; Zakharov, A. A.; Starke, U. Quasi-free-standing epitaxial graphene on SiC obtained by hydrogen intercalation. *Phys. Rev. Lett.* **2009**, *103*, 246804.

[31] Sutter, P.; Sadowski, J. T.; Sutter, E. A. Chemistry under cover: Tuning metal−graphene interaction by reactive intercalation. *J. Am. Chem. Soc.* **2010**, *132*, 8175–8179.

[32] Duong, D. L.; Han, G. H.; Lee, S. M.; Gunes, F.; Kim, E. S.; Kim, S. T.; Kim, H.; Ta, Q. H.; So, K. P.; Yoon, S. J. et al. Probing graphene grain boundaries with optical microscopy. *Nature* **2012**, *490*, 235–239.

[33] Feng, X. F.; Maier, S.; Salmeron, M. Water splits epitaxial graphene and intercalates. *J. Am. Chem. Soc.* **2012**, *134*, 5662–5668.

[34] Grånäs, E.; Andersen, M.; Arman, M. A.; Gerber, T.; Hammer, B.; Schnadt, J.; Andersen, J. N.; Michely, T.; Knudsen, J. CO intercalation of graphene on Ir(111) in the millibar regime. *J. Phys. Chem. C* **2013**, *117*, 16438–16447.

[35] Zhang, Y. H.; Weng, X. F.; Li, H.; Li, H. B.; Wei, M. M.; Xiao, J. P.; Liu, Z.; Chen, M. S.; Fu, Q.; Bao, X. H. Hexagonal boron nitride cover on Pt(111): A new route to tune molecule–metal interaction and metal-catalyzed reactions. *Nano Lett.* **2015**, *15*, 3616–3623.

[36] Cui, Y.; Gao, J. F.; Jin, L.; Zhao, J. J.; Tan, D. L.; Fu, Q.; Bao, X. H. An exchange intercalation mechanism for the formation of a two-dimensional Si structure underneath graphene. *Nano Res.* **2012**, *5*, 352–360.

[37] Hao, Y. F.; Wang, L.; Liu, Y. Y.; Chen, H.; Wang, X. H.; Tan, C.; Nie, S.; Suk, J. W.; Jiang, T. F.; Liang, T. F. et al. Oxygen-activated growth and bandgap tunability of large single-crystal bilayer graphene. *Nat. Nanotechnol.* **2016**, *11*, 426–431.

[38] Zhou, S. S.; Gan, L.; Wang, D. L.; Li, H. Q.; Zhai, T. Y. Space-confined vapor deposition synthesis of two dimensional materials. *Nano Res.* **2018**, *11*, 2909–2931.

[39] Li, Q. Y.; Chou, H.; Zhong, J. H.; Liu, J. Y.; Dolocan, A.; Zhang, J. Y.; Zhou, Y. Y.; Ruoff, R. S.; Chen, S. S.; Cai, W. W. Growth of adlayer graphene on Cu studied by carbon isotope labeling. *Nano Lett.* **2013**, *13*, 486–490.

[40] Yang, Y.; Fu, Q.; Li, H. B.; Wei, M. M.; Xiao, J. P.; Wei, W.; Bao, X. H. Creating a nanospace under an h-BN cover for adlayer growth on nickel(111). *ACS Nano* **2015**, *9*, 11589–11598.

[41] Al Balushi, Z. Y.; Wang, K.; Ghosh, R. K.; Vilá, R. A.; Eichfeld, S. M.; Caldwell, J. D.; Qin, X. Y.; Lin, Y. C.; DeSario, P. A.; Stone, G. et al. Two-dimensional gallium nitride realized via graphene encapsulation. *Nat. Mater.* **2016**, *15*, 1166–1171.

[42] Zhou, X. B.; Qi, Y.; Shi, J. P.; Niu, J. J.; Liu, M. X.; Zhang, G. H.; Li, Q. C.; Zhang, Z. P.; Hong, M.; Ji, Q. Q. et al. Modulating the electronic properties of monolayer graphene using a periodic quasi-one-dimensional potential generated by hex-reconstructed Au(001). *ACS Nano* **2016**, *10*, 7550–7557.

[43] Jiang, S. L.; Hong, M.; Wei, W.; Zhao, L. Y.; Zhang, N.; Zhang, Z. P.; Yang, P. F.; Gao, N.; Zhou, X. B.; Xie, C. Y. et al. Direct synthesis and *in situ* characterization of monolayer parallelogrammic rhenium diselenide on gold foil. *Commun. Chem.* **2018**, *1*, 17.

[44] Rutter, G. M.; Crain, J. N.; Guisinger, N. P.; Li, T.; First, P. N.; Stroscio, J. A. Scattering and interference in epitaxial graphene. *Science* **2007**, *317*, 219–222.

[45] Gong, C. H.; Zhang, Y. X.; Chen, W.; Chu, J. W.; Lei, T. Y.; Pu, J. R.; Dai, L. P.; Wu, C. Y.; Cheng, Y. H.; Zhai, T. Y. et al. Electronic and optoelectronic applications based on 2D novel anisotropic transition metal dichalcogenides. *Adv. Sci.* **2017**, *4*, 1700231.

[46] Hafeez, M.; Gan, L.; Saleem Bhatti, A.; Zhai, T. Y. Rhenium dichalcogenides (ReX_2, X = S or Se): An emerging class of TMDs family. *Mater. Chem. Front.* **2017**, *1*, 1917–1932.

[47] Parkinson, B. A.; Ren, J.; Whangbo, M. H. Relationship of STM and AFM images to the local density of states in the valence and conduction bands of rhenium selenide ($ReSe_2$). *J. Am. Chem. Soc.* **1991**, *113*, 7833–7837.

[48] Zhong, H. X.; Gao, S. Y.; Shi, J. J.; Yang, L. Quasiparticle band gaps, excitonic effects, and anisotropic optical properties of the monolayer distorted 1T diamond-chain structures ReS_2 and $ReSe_2$. *Phys. Rev. B* **2015**, *92*, 115438.

[49] Kelty, S. P.; Ruppert, A. F.; Chianelli, R. R.; Ren, J.; Whangbo, M. H. Scanning probe microscopy study of layered dichalcogenide ReS_2. *J. Am. Chem. Soc.* **1994**, *116*, 7857–7863.

[50] Zhang, E. Z.; Wang, P.; Li, Z.; Wang, H. F.; Song, C. Y.; Huang, C.; Chen, Z. G.; Yang, L.; Zhang, K. K.; Lu, S. H. et al. Tunable ambipolar polarization-sensitive photodetectors based on high-anisotropy $ReSe_2$ nanosheets. *ACS Nano* **2016**, *10*, 8067–8077.

[51] Hafeez, M.; Gan, L.; Li, H. Q.; Ma, Y.; Zhai, T. Y. Chemical vapor deposition synthesis of ultrathin hexagonal $ReSe_2$ flakes for anisotropic Raman property and optoelectronic application. *Adv. Mater.* **2016**, *28*, 8296–8301.

[52] Cui, F. F.; Feng, Q. L.; Hong, J. H.; Wang, R. Y.; Bai, Y.; Li, X. B.; Liu, D. Y.; Zhou, Y.; Liang, X.; He, X. X. et al. Synthesis of large-size 1T' $ReS_{2x}Se_{2(1-x)}$ alloy monolayer with tunable bandgap and carrier type. *Adv. Mater.* **2017**, *29*, 1705015.

[53] Shi, J. P.; Tong, R.; Zhou, X. B.; Gong, Y.; Zhang, Z. P.; Ji, Q. Q.; Zhang, Y.; Fang, Q.; Gu, L. Y.; Wang, X. N. et al. Temperature-mediated selective growth of MoS_2/WS_2 and WS_2/MoS_2 vertical stacks on Au foils for direct photocatalytic applications. *Adv. Mater.* **2016**, *28*, 10664–10672.

[54] Gao, T.; Song, X. J.; Du, H. W.; Nie, Y. F.; Chen, Y. B.; Ji, Q. Q.; Sun, J. Y.; Yang, Y. L.; Zhang, Y. F.; Liu, Z. F. Temperature-triggered chemical switching growth of in-plane and vertically stacked graphene-boron nitride heterostructures. *Nat. Commun.* **2015**, *6*, 6835.

[55] Fu, Q.; Bao, X. H. Surface chemistry and catalysis confined under two-dimensional materials. *Chem. Soc. Rev.* **2017**, *46*, 1842–1874.

[56] Preobrajenski, A. B.; Ng, M. L.; Vinogradov, A. S.; Mårtensson, N. Controlling graphene corrugation on lattice-mismatched substrates. *Phys. Rev. B* **2008**, *78*, 073401.

[57] Yao, Y. X.; Fu, Q.; Zhang, Y. Y.; Weng, X. F.; Li, H.; Chen, M. S.; Jin, L.; Dong, A. Y.; Mu, R. T.; Jiang, P. et al. Graphene cover-promoted metal-catalyzed reactions. *Proc. Natl. Acad. Sci. USA* **2014**, *111*, 17023–17028.

[58] Lyo, I. W.; Avouris, P. Field-induced nanometer- to atomic-scale manipulation of silicon surfaces with the STM. *Science* **1991**, *253*, 173–176.

[59] Eigler, D. M.; Lutz, C. P.; Rudge, W. E. An atomic switch realized with the scanning tunnelling microscope. *Nature* **1991**, *352*, 600–603.

[60] Rubio-Verdú, C.; Sáenz-Arce, G.; Martinez-Asencio, J.; Milan, D. C.; Moaied, M.; Palacios, J. J.; Caturla, M. J.; Untiedt, C. Graphene flakes obtained by local electro-exfoliation of graphite with a STM tip. *Phys. Chem. Chem. Phys.* **2017**, *19*, 8061–8068.

[61] Rutter, G. M.; Guisinger, N. P.; Crain, J. N.; Jarvis, E. A. A.; Stiles, M. D.; Li, T.; First, P. N.; Stroscio, J. A. Imaging the interface of epitaxial graphene with silicon carbide via scanning tunneling microscopy. *Phys. Rev. B* **2007**, *76*, 235416.

[62] He, K. T.; Koepke, J. C.; Barraza-Lopez, S.; Lyding, J. W. Separation-dependent electronic transparency of monolayer graphene membranes on

III−V semiconductor substrates. *Nano Lett*. **2010**, *10*, 3446–3452.
[63] Xu, Y.; He, K. T.; Schmucker, S. W.; Guo, Z.; Koepke, J. C.; Wood, J. D.; Lyding, J. W.; Aluru, N. R. Inducing electronic changes in graphene through silicon (100) substrate modification. *Nano Lett*. **2011**, *11*, 2735–2742.
[64] Jin, L.; Fu, Q.; Mu, R. T.; Tan, D. L.; Bao, X. H. Pb intercalation underneath a graphene layer on Ru(0001) and its effect on graphene oxidation. *Phys*. *Chem*. *Chem*. *Phys*. **2011**, *13*, 16655–16660.
[65] Emtsev, K. V.; Zakharov, A. A.; Coletti, C.; Forti, S.; Starke U. Ambipolar doping in quasifree epitaxial graphene on SiC(0001) controlled by Ge intercalation. *Phys*. *Rev*. *B* **2011**, *84*, 125423.
[66] Rut'kov, E. V.; Gall', N. R. Role of edge atoms of graphene islands on metals in nucleation, growth, alkali metal intercalation. *Phys*. *Solid State* **2009**, *51*, 1738–1743.
[67] Mu, R. T.; Fu, Q.; Jin, L.; Yu, L.; Fang, G. Z.; Tan, D. L.; Bao, X. H. Visualizing chemical reactions confined under graphene. *Angew*. *Chem*., *Int*. *Ed*. **2012**, *51*, 4856–4859.
[68] Shi, J. P.; Zhou, X. B.; Han, G. F.; Liu, M. X.; Ma, D. L.; Sun, J. Y.; Li, C.; Ji, Q. Q.; Zhang, Y.; Song, X. J. et al. Narrow-gap quantum wires arising from the edges of monolayer MoS_2 synthesized on graphene. *Adv*. *Mater*. *Interfaces* **2016**, *3*, 1600332.
[69] Kresse, G.; Furthmüller, J. Efficient iterative schemes for *ab initio* total-energy calculations using a plane-wave basis set. *Phys*. *Rev*. *B* **1996**, *54*, 11169.
[70] Perdew, J. P.; Burke, K.; Ernzerhof, M. Generalized gradient approximation made simple. *Phys*. *Rev*. *Lett*. **1996**, *77*, 3865.
[71] Blöchl, P. E. Projector augmented-wave method. *Phys*. *Rev*. *B* **1994**, *50*, 17953.
[72] Kresse, G.; Joubert, D. From ultrasoft pseudopotentials to the projector augmented-wave method. *Phys*. *Rev*. *B* **1999**, *59*, 1758–1775.
[73] Tkatchenko, A.; Scheffler, M. Accurate molecular van der Waals interactions from ground-state electron density and free-atom reference data. *Phys*. *Rev*. *Lett*. **2009**, *102*, 073005.